

## *Electronic Supporting Information*

### **Polyoxometalates with separate lacuna sites**

Wenyan Wang,<sup>a</sup> Natalya V. Izarova,<sup>a,b</sup> Jan van Leusen,<sup>a</sup> and Paul Kögerler\*<sup>a,b</sup>

<sup>a</sup> Institute of Inorganic Chemistry, RWTH Aachen University, D-52074 Aachen

<sup>b</sup> Jülich-Aachen Research Alliance (JARA-FIT) and Peter Grünberg Institute – PGI-6,  
Forschungszentrum Jülich, D-52425 Jülich, Germany

## Table of Contents

I. Synthesis details .....	3
I.1. Starting Materials.....	3
I.2. Instruments .....	3
I.3. Synthetic procedures.....	4
II. X-ray crystallography .....	6
II.1. Single-crystal X-ray diffraction analysis.....	6
II.2. Powder X-ray diffraction.....	7
III. Additional structural figures .....	12
IV. FT-IR spectroscopy .....	15
V. Thermogravimetric analysis .....	17
VI. NMR spectroscopy .....	19
VII. UV-Vis spectroscopy .....	22
VIII. Electrochemical studies .....	24
IX. Magnetochemical studies .....	29
X. References.....	33

# I. Synthesis details

## I.1. Starting Materials

The precursors  $K_{10}[\alpha_2\text{-P}_2\text{W}_{17}\text{O}_{61}] \cdot 20\text{H}_2\text{O}$  and  $K_5\text{H}[\text{P}_2\text{W}_{17}\text{O}_{61}(\text{P}(=\text{O})\text{C}_6\text{H}_5)_2] \cdot 4\text{C}_4\text{H}_9\text{NO}$  were prepared as previously reported,<sup>[1,2]</sup> and their identity was confirmed by IR spectroscopy. All other reagents were of analytical grade and were obtained from commercial sources and used without further purification.

## I.2. Instruments

Elemental analyses (inductively coupled plasma atomic emission spectroscopy (ICP-OES) and C, H, and N) were obtained from the Central Institute for Engineering, Electronics and Analytics (ZEA-3), Forschungszentrum Jülich GmbH (Jülich, Germany). Thermogravimetric/differential thermal analysis (TGA/DTA) measurements were carried out with a Netzsch STA 409 C / CD in a dry  $\text{N}_2$  flux ( $60 \text{ mL min}^{-1}$ ) at a heating rate of  $5 \text{ K min}^{-1}$ . FT-IR spectra were recorded on Bruker Vertex 70 and Avatar 360 spectrometers using KBr pellets.

UV-Vis spectra were recorded in  $0.5 \text{ M Li}_2\text{SO}_4$  solutions with pH 2.5 (prepared by addition of solid LiOH into  $0.5 \text{ M H}_2\text{SO}_4$  solution in water until pH became 2.5) in the range of 200–1000 nm on a UV-2600 Shimadzu spectrophotometer. Cyclic voltammograms were recorded on a saturated ( $0.5 \text{ mM}$ ) solutions of **CsK-1** and **CsK-2** in  $1 \text{ M LiOAc}$  buffer (pH 3.8), prepared by addition of solid LiOH in  $1 \text{ M HOAc}$  solution in water until pH 3.8 (RT), using a SP-150 potentiostat (Bio Logic Science Instruments) controlled by EC-Lab software. The conventional three-electrode electrochemical cell included a glassy carbon working electrode with a 3 mm diameter, a platinum wire counter electrode and an aqueous Ag/AgCl ( $3 \text{ M NaCl}$ ). The solutions were thoroughly deaerated with pure argon and kept under a positive Ar pressure during the experiments. Alumina powder was used for the cleaning of the working electrode which was then thoroughly rinsed with deionized water. Redox potentials were defined from the average values of the anodic and cathodic peak potentials and reported vs. the Ag/AgCl reference electrode.

$^1\text{H}$  and  $^{31}\text{P}$  NMR spectra were recorded at room temperature in 5 mm tubes using a Bruker Avance 600 MHz spectrometer equipped with a prodigy probe operating at 600.15 MHz for  $^1\text{H}$

and 242.95 MHz for  $^{31}\text{P}$ . The chemical shifts were referenced according to  $\text{Si}(\text{CH}_3)_4$  ( $^1\text{H}$ ) and 85 %  $\text{H}_3\text{PO}_4$  ( $^{31}\text{P}$ ). All chemical shifts downfield of the reference are reported as positive values.

Magnetic data of the products **CsK-2** (for diamagnetic correction purposes) and **CsK-1** were recorded using a Quantum Design MPMS-5XL SQUID magnetometer. The polycrystalline samples were compacted and immobilized into cylindrical PTFE capsules. The dc data were acquired as a function of the magnetic field (0.1–5.0 T at 2.0 K) and temperature (2.0–290 K at 0.1 T). The ac data were measured at zero and different static bias fields as a function of temperature (1.9–50 K) and frequency (3–997 Hz) applying an amplitude of  $B_{\text{ac}} = 3$  G. All data were corrected for the diamagnetic contributions of the sample holders and compounds using the molar weight method, and further corrected by taking into account the data from **CsK-2** (see below, **Figure S21**) ultimately yielding:  $\chi_{\text{m,dia}} / 10^{-4} \text{ cm}^3 \text{ mol}^{-1} = -0.89$  (**CsK-2**),  $-2.54$  (**CsK-1**).

### I.3. Synthetic procedures

#### I.3.1. Synthesis of $\text{Cs}_{7.5}\text{K}_{0.5}[\{(\text{H}_2\text{O})_7\text{Dy}^{\text{III}}_2(\alpha_2, \alpha_2' - \text{P}_2\text{W}_{16}\text{O}_{60})(\text{C}_6\text{H}_5\text{PO})_2\}_2] \cdot 42\text{H}_2\text{O}$ (**CsK-1**)

A solid sample of  $\text{Dy}(\text{NO}_3)_3 \cdot 5\text{H}_2\text{O}$  (0.009 g, 0.02 mmol) was added into a solution of  $\text{K}_5\text{H}[\alpha_2 - \text{P}_2\text{W}_{17}\text{O}_{61}(\text{P}(=\text{O})\text{C}_6\text{H}_5)_2] \cdot 4\text{C}_4\text{H}_9\text{NO}$  (0.10 g, 0.01 mmol) in  $\text{H}_2\text{O}$  (10 mL) under vigorous stirring. The obtained reaction mixture was then stirred at room temperature for 3 hours while protected from sunlight. Subsequently, 0.5 M  $\text{CsCl}$  solution in water (3 drops) was added to the reaction mixture and the vigorous stirring was continued for another 30 minutes. After that, the resulting mixture ( $\text{pH} \approx 2.3$ ) was filtered and left for evaporation in air in an open vial being protected from sunlight. Pale-blue rhombic crystals of **CsK-1** were collected after two weeks by vacuum filtration, thoroughly washed with cold water and dried in air. Yield: 0.013 g (10.8 % based on W).

Elemental analysis, mass %, calculated for  $\text{C}_{24}\text{H}_{132}\text{Cs}_{7.5}\text{Dy}_4\text{K}_{0.5}\text{O}_{180}\text{P}_8\text{W}_{32}$  (found): C, 2.60 (2.66); H, 1.20 (1.2); Cs, 8.98 (8.95); Dy, 5.86 (5.77); K, 0.18 (0.14); P, 2.23 (2.14); W, 53.01 (49.7). FT-IR (2 % KBr pellet),  $\nu_{\text{max}} / \text{cm}^{-1}$ : 3417 (m, br); 1616 (m); 1488 (w); 1436 (w); 1384 (m); 1170 (m); 1139 (s); 1097 (s); 1061 (s); 1026 (s); 985 (s); 940 (s); 846 (s); 773 (s); 700 (s); 635 (s); 590 (s); 561 (s); 530 (s); 484 (s); 463 (s). UV-Vis (0.5 M  $\text{Li}_2\text{SO}_4$  solution):  $\lambda = 201$  nm,  $\epsilon = 4.24 \times 10^5 \text{ M}^{-1} \text{ cm}^{-1}$ ;  $\lambda = 256$  nm,  $\epsilon = 9.14 \times 10^4 \text{ M}^{-1} \text{ cm}^{-1}$ .

### I.3.2. Synthesis of $\text{Cs}_{7.5}\text{K}_{0.5}[\{(\text{H}_2\text{O})_{7.7}\text{Y}^{\text{III}}_2(\alpha_2, \alpha_2' \text{-P}_2\text{W}_{16}\text{O}_{60})(\text{C}_6\text{H}_5\text{PO})_2\}_2] \cdot 38.6 \text{H}_2\text{O}$ (CsK-2)

The pale-blue crystalline material of **CsK-2** was prepared in a similar way using  $\text{Y}(\text{NO}_3)_3 \cdot 6 \text{H}_2\text{O}$  (0.008 g, 0.02 mmol) instead of  $\text{Dy}(\text{NO}_3)_3 \cdot 5 \text{H}_2\text{O}$ . Yield: 0.011 g (9.4 % based on W).

Elemental analysis, mass %, calculated for  $\text{C}_{24}\text{H}_{128}\text{Cs}_{7.5}\text{Y}_4\text{K}_{0.5}\text{O}_{178}\text{P}_8\text{W}_{32}$  (found): C, 2.68 (2.8); H, 1.20 (1.21); Cs, 9.26 (9.3); Y, 3.3 (3.09); K, 0.18 (0.15); P, 2.30 (2.09); W, 54.64 (50.5). FT-IR (2 % KBr pellet),  $\nu_{\text{max}} / \text{cm}^{-1}$ : 3417 (m, br); 1619 (m); 1488 (w); 1436 (w); 1384 (m); 1173 (m); 1139 (m); 1097 (s); 1061 (s); 1025 (s); 985(s); 940 (s); 848 (s); 774 (s); 700(s); 635 (s); 590(s); 561 (s); 530 (s); 484(s); 463(s). UV-Vis (0.5 M  $\text{Li}_2\text{SO}_4$  solution):  $\lambda = 200 \text{ nm}$ ,  $\varepsilon = 3.68 \times 10^5 \text{ M}^{-1}\text{cm}^{-1}$ ;  $\lambda = 256 \text{ nm}$ ,  $\varepsilon = 7.82 \times 10^4 \text{ M}^{-1}\text{cm}^{-1}$ .

## II. X-ray crystallography

### II.1. Single-crystal X-ray diffraction analysis

Single-crystal X-ray diffraction data on **CsK-1** and **CsK-2** were collected on a STOE STADIVARI diffractometer at 100 K with MoK $\alpha$  radiation ( $\lambda = 0.71073 \text{ \AA}$ ). The crystals were mounted in a Hampton cryoloop with Paratone-N oil to prevent water loss. Absorption corrections were done by Gaussian integration using STOE X-Red32 software<sup>[3]</sup> and afterwards scaling of reflection intensities was performed within STOE LANA.<sup>[4]</sup>

The structures were solved by direct methods and refined by full-matrix least-squares method against  $|F|^2$  with anisotropic thermal parameters for all heavy atoms (Dy / Y, P, W, Cs and K) employing the SHELXTL software package.<sup>[5]</sup> ISOR restrictions had to be applied for some disordered Cs and K positions with low site occupancy factors (s. o. f.). Hydrogen atoms of water molecules were not located. Hydrogen atoms of phenyl rings were placed in geometrically calculated positions.

One of the two phenyl rings in the asymmetric unit (half of the molecule) in the both structures exhibits rotational disorder. One of the possible positions for this phenyl ring has been located with s. o. f. of 0.69 (**CsK-1**) and 0.58 (**CsK-2**), while the other orientations could not be found from the electron density map. The relative s. o. f. for the disordered positions of O atoms of water molecules (from the co-crystallized solvent and coordinated to Dy2 (**CsK-1**) or Y2 (**CsK-2**) centers), cesium and potassium counterions were either refined applying a combination of PART and EADP commands or were first refined in an isotropic approximation with  $U_{\text{iso}} = 0.05$  and then fixed at the obtained values and refined without restrictions of the thermal parameters.

Due to severe disorder we were not able to locate part of solvent H<sub>2</sub>O molecules in all the structures and even some Cs<sup>+</sup> positions in **CsK-2** structure (only ~7.0 instead of expected 7.5 Cs<sup>+</sup> counterions were found), which is a typical problem in the polyoxotungstate crystallography. However, for the overall consistency, the final formulae in the CIFs correspond to the composition of the bulk materials determined by elemental analysis and TGA.

The relatively high residual electron density peaks in the structures ( $3.0 - 5.4 \text{ e\AA}^{-3}$ ) are located in the proximity of the W and Cs centers and should correspond to some residual absorption artefacts. Rather high  $R_{\text{int}}$  factors (0.14 for **CsK-1** and 0.16 for **CsK-2**) reflect possible twinning issues (as the crystals are thin plates).

Additional crystallographic data are summarized in **Table S1**. Further details on the crystal structures investigation can be obtained, free of charge, on application to CCDC, 12 Union Road, Cambridge CB2 1EZ, UK: <http://www.ccdc.cam.ac.uk/>, e-mail: [data\\_request@ccdc.cam.ac.uk](mailto:data_request@ccdc.cam.ac.uk), or fax: +441223 336033 upon quoting CCDC numbers 2019292 (**CsK-1**) and 2019293 (**CsK-2**). The selected bond lengths in **1** and **2** are shown in **Table S2**.

## II.2. Powder X-ray diffraction

PXRD patterns for **CsK-1** (**Figure S1**) and **CsK-2** (**Figure S2**) were recorded with a STADI P powder diffractometer from STOE (Darmstadt, Germany). The experiments were performed on flat samples in a transmission geometry using a Cu anode ( $K\alpha_1$ ,  $\lambda = 1.54059\text{\AA}$ ; 40 kV, 30 mA) and a focusing Ge-monochromator (Johann-type) at room temperature. The omega angle was held at  $55^\circ$  and the data were recorded with an image plate detector ( $140^\circ$  in  $2\Theta$ , stepwidth  $0.015^\circ$ ). The exposure times were between 3600 s and 7200 s.

For the measurements the crystals of the respective sample were mortared in a small amount of mother liquor to prevent a removal of co-crystallized solvent molecules and a subsequent crystallinity loss and placed to a sample holder together with a small amount of mother solution. At that, the quality of mortaring (*e. g.* achievable of the random orientation of crystals in the sample holder) played an important role for the quality of the obtained XRD patterns.

The observed PXRD patterns show very good fit to the curves simulated from the single crystal X-ray data and, thus, confirm the bulk purity of the **CsK-1** and **CsK-2** materials. Sharpness and high intensity of the reflexes observed below  $2\theta = 10^\circ$  indicate a high crystallinity of the measured samples.

**Figure S3** shows the morphology of the crystals for the studied materials on the example of **CsK-1** (the crystal shape and sizes for the crystals of **CsK-2** is very similar).

**Table S1.** Crystal data and structure refinement for **CsK-1** and **CsK-2**.

Sample	CsK-1	CsK-2
Empirical formula	C <sub>24</sub> H <sub>132</sub> Cs <sub>7.5</sub> Dy <sub>4</sub> K <sub>0.5</sub> O <sub>180</sub> P <sub>8</sub> W <sub>32</sub>	C <sub>24</sub> H <sub>128</sub> Cs <sub>7.5</sub> K <sub>0.5</sub> O <sub>178</sub> P <sub>8</sub> W <sub>32</sub> Y <sub>4</sub>
Formula weight /g mol <sup>-1</sup>	11098.62	10768.23
Crystal system	Triclinic	Triclinic
Space group	<i>P</i> -1	<i>P</i> -1
<i>a</i> / Å	12.757(3)	12.902(3)
<i>b</i> / Å	14.616(3)	14.649(3)
<i>c</i> / Å	24.915(5)	24.956(5)
$\alpha$	73.84(3)°	73.56(3)°
$\beta$	86.54(3)°	86.69(3)°
$\gamma$	79.70(3)°	79.61(3)°
Volume / Å <sup>3</sup>	4389.8(17)	4449.3(17)
<i>Z</i>	1	1
<i>D</i> <sub>calc</sub> / g cm <sup>-3</sup>	4.198	4.019
Absorption coefficient / mm <sup>-1</sup>	24.287	23.592
<i>F</i> (000)	4890	4762
Crystal size / mm <sup>3</sup>	0.03 × 0.09 × 0.09	0.03 × 0.105 × 0.20
Theta range for data collection	2.33° – 25.35°	2.32° – 25.03°
Completeness to $\theta_{\max}$	99.9 %	99.9 %
Index ranges	-15 < <i>h</i> < 15, -16 < <i>k</i> < 17, -24 < <i>l</i> < 30	-15 < <i>h</i> < 15, -17 < <i>k</i> < 17, -28 < <i>l</i> < 29
Reflections collected	89602	90921
Independent reflections	16066	15715
<i>R</i> <sub>int</sub>	0.1472	0.1635
Observed ( <i>I</i> > 2σ( <i>I</i> ))	9318	8347
Absorption correction	Gaussian integration	
<i>T</i> <sub>min</sub> / <i>T</i> <sub>max</sub>	0.1377 / 0.5079	0.0898 / 0.4149
Data / restraints / parameters	16066 / 36 / 634	15715 / 42 / 655
Goodness-of-fit on F <sup>2</sup>	0.998	1.013
<i>R</i> <sub>1</sub> , <i>wR</i> <sub>2</sub> ( <i>I</i> > 2σ( <i>I</i> ))	<i>R</i> <sub>1</sub> = 0.0870, <i>wR</i> <sub>2</sub> = 0.2206	<i>R</i> <sub>1</sub> = 0.0815, <i>wR</i> <sub>2</sub> = 0.1959
<i>R</i> <sub>1</sub> , <i>wR</i> <sub>2</sub> (all data)	<i>R</i> <sub>1</sub> = 0.1357, <i>wR</i> <sub>2</sub> = 0.2469	<i>R</i> <sub>1</sub> = 0.1434, <i>wR</i> <sub>2</sub> = 0.2201
Largest diff. peak and hole / e Å <sup>-3</sup>	4.717 / -5.408	3.123 / -3.355

**Table S2.** Selected bond lengths (Å) in **1** and **2** as determined from the crystal structures of **CsK-1** and **CsK-2**.

Bond type	Bond length / Å	
	CsK-1	CsK-2
W=O <sub>t</sub>	1.63(2) – 1.76(2)	1.64(2) – 1.74(2)
W–μ <sub>2</sub> -O (W–O–W)	1.774(18) – 2.142(18)	1.727(18) – 2.180(17)
W–μ <sub>2</sub> -O (W–O–M)	1.709(17) – 1.78(2)	1.72(2) – 1.75(2)
W–μ <sub>2</sub> -O (W–O–P <sub>L</sub> )	2.053(17) – 2.071(18)	2.035(18) – 2.07(2)
W–μ <sub>3</sub> -O (2W+P)	2.252(17) – 2.38(2)	2.243(18) – 2.382(18)
P–μ <sub>3</sub> -O (2W+P)	1.53(2) – 1.57(2)	1.498(18) – 1.563(18)
P <sub>L</sub> –μ <sub>2</sub> -O (P <sub>L</sub> –O–W)	1.51(2) – 1.539(18)	1.51(2) – 1.558(19)
P <sub>L</sub> –μ <sub>2</sub> -O (P <sub>L</sub> –O–M)	1.49(2) – 1.50(3)	1.44(2) – 1.48(2)
P <sub>L</sub> –C	1.820(18) – 1.83(2)	1.82(2) – 1.853(18)
M–μ <sub>2</sub> -O (M–O–W)	2.336(19) – 2.43(2)	2.32(2) – 2.40(2)
M–μ <sub>2</sub> -O (M–O–P <sub>L</sub> )	2.27(3) – 2.280(19)	2.27(2) – 2.29(2)
M–O <sub>H2O</sub>	2.25(5) – 2.47(3)	2.26(6) – 2.67(8)

Dy-compared 2nd good

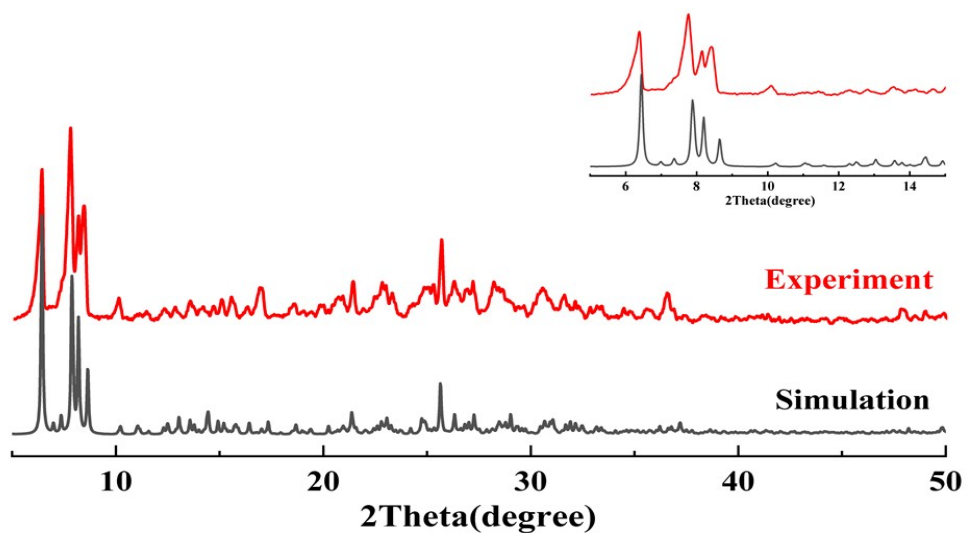


**Figure S1** Experimental (red line) and calculated from the single crystal data (black line) powder X-ray patterns for CsK-1. The inset highlights the small angles area.

Y compared

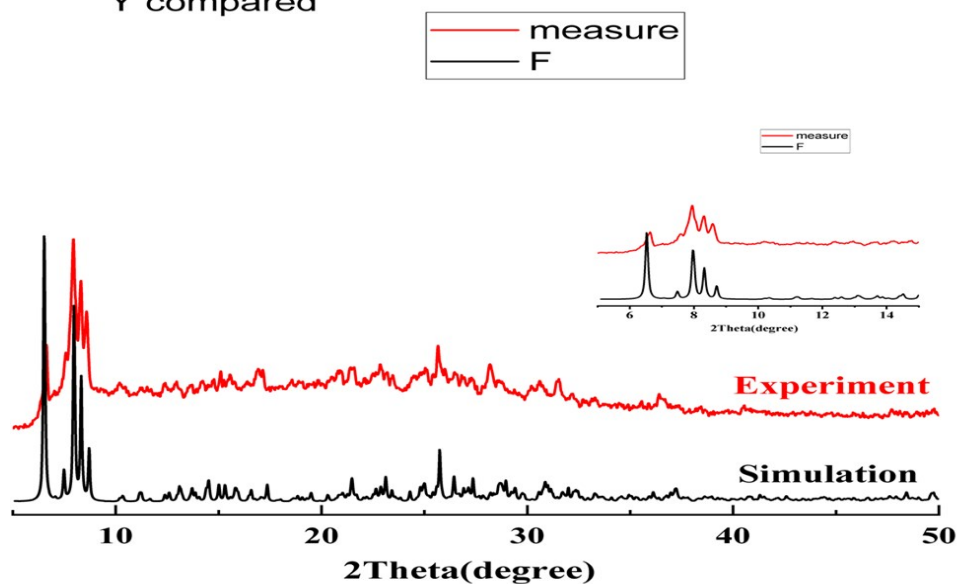


**Figure S2** Experimental (red line) and calculated from the single crystal data (black line) powder X-ray patterns for CsK-2. The inset highlights the small angles area.

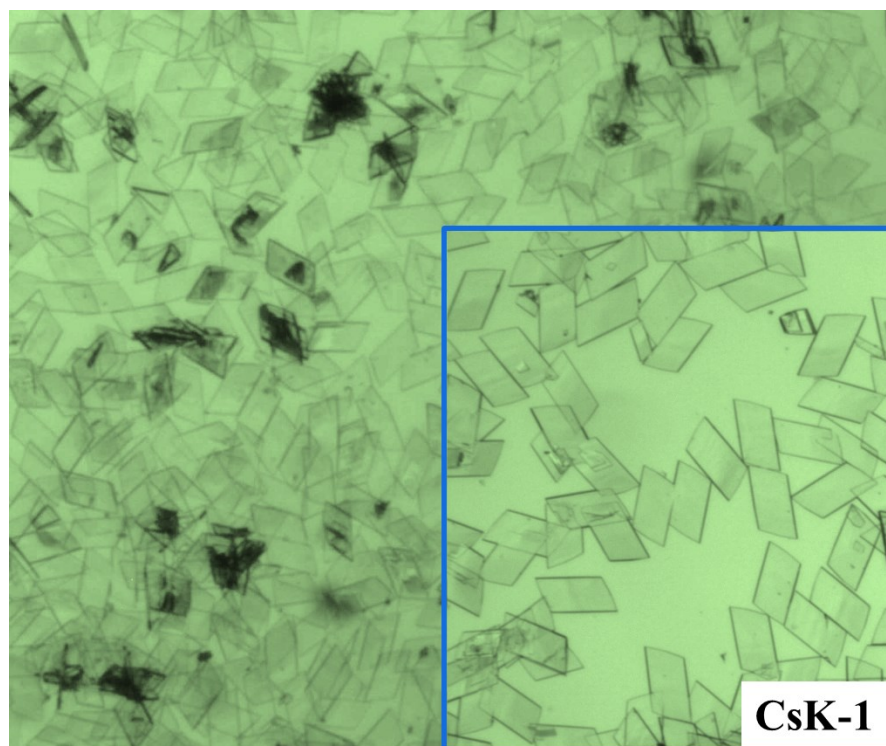


**Figure S3.** The morphology of the crystals of **CsK-1**.

### III. Additional structural figures

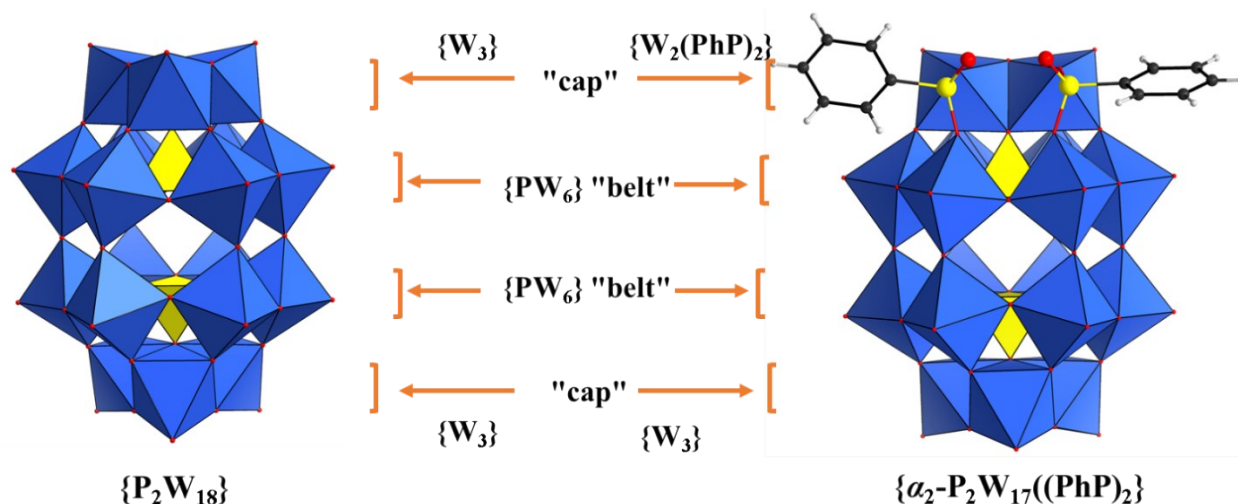


**Figure S4.** Structural aspects of the Wells-Dawson-type phosphotungstate  $[\alpha\text{-P}_2\text{W}_{18}\text{O}_{62}]^{6-}$  ( $\{\alpha\text{-P}_2\text{W}_{18}\}$ ; left) and its phenylphosphonate-decorated monolacunary derivative  $[\alpha_2\text{-P}_2\text{W}_{17}\text{O}_{61}(\text{C}_6\text{H}_5\text{PO})_2]^{6-}$  ( $\{\alpha_2, \alpha_2'\text{-P}_2\text{W}_{17}(\text{PhP})_2\}$ ; right). Color code:  $\text{PO}_4$ : yellow tetrahedra,  $\text{WO}_6$ : blue octahedra; O: red spheres.

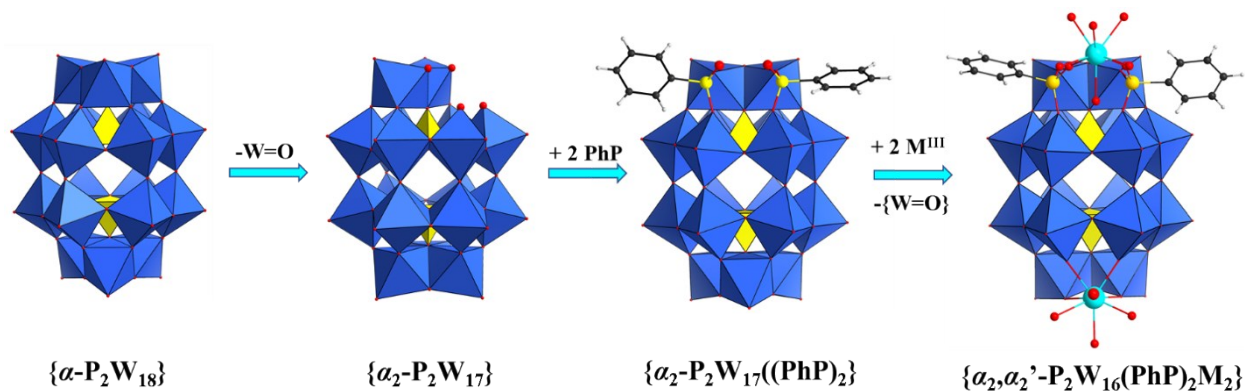


**Figure S5.** Structural interrelations between Wells-Dawson-type polyanion  $[\alpha\text{-P}_2\text{W}_{18}\text{O}_{62}]^{6-}$  ( $\{\alpha\text{-P}_2\text{W}_{18}\}$ ), its monolacunary derivative  $[\alpha_2\text{-P}_2\text{W}_{17}\text{O}_{61}]^{10-}$  ( $\{\alpha_2\text{-P}_2\text{W}_{17}\}$ ), the phenylphosphonate-functionalized precursor  $[\alpha_2\text{-P}_2\text{W}_{17}\text{O}_{61}(\text{C}_6\text{H}_5\text{PO})_2]^{6-}$  ( $\{\alpha_2\text{-P}_2\text{W}_{17}(\text{PhP})_2\}$ ) and the monomeric unit  $\{(\text{H}_2\text{O})_9\text{M}^{\text{III}}_2(\alpha_2, \alpha_2'\text{-P}_2\text{W}_{16}\text{O}_{60})(\text{C}_6\text{H}_5\text{PO})_2\}^{4-}$  ( $\{\alpha_2, \alpha_2'\text{-P}_2\text{W}_{16}(\text{PhP})_2M_2\}$ ) observed in the structures of **CsK-1** and **CsK-2**. Color code:  $\{\text{PO}_4\}$ : yellow tetrahedra,  $\{\text{WO}_6\}$ : blue octahedra; P: yellow, M: cyan-blue, O: red, C: black, H: white spheres.

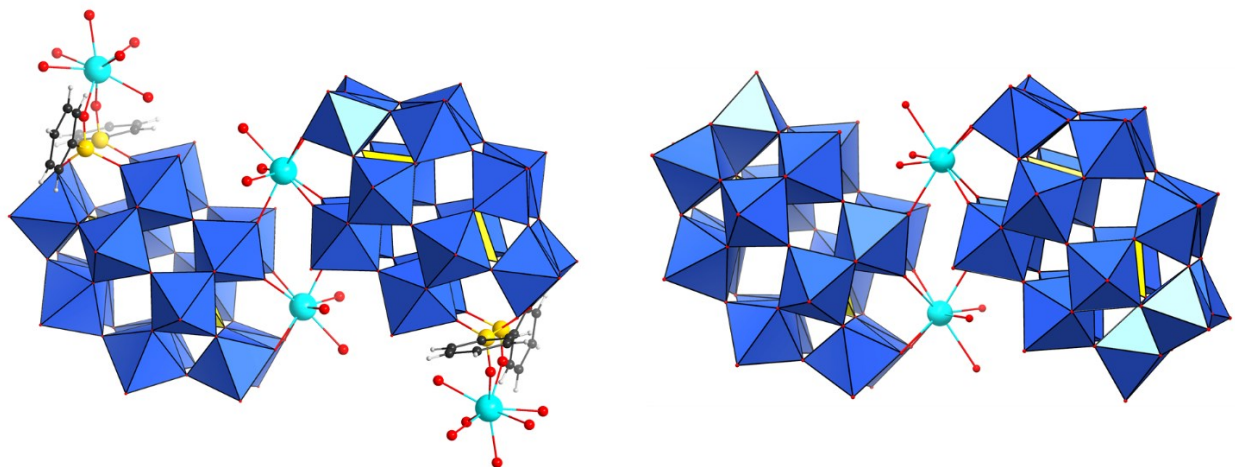


**Figure S6.** Comparison between the structures of  $[\{(H_2O)_9M^{III}_2(\alpha_2, \alpha_2'-P_2W_{16}O_{60})(C_6H_5PO)_2\}_2]^{8-}$  ( $M = Dy$  (**1**) and  $Y$  (**2**); left) and  $[\{Ln(H_2O)_3(\alpha_2-P_2W_{17}O_{61})\}_2]^{14-}$  ( $Ln =$  lanthanide ion; right). Color code:  $\{PO_4\}$ : yellow tetrahedra,  $\{WO_6\}$ : blue octahedra;  $M$  or  $Ln$ : cyan-blue,  $O$ : red,  $C$ : black,  $H$ : white spheres

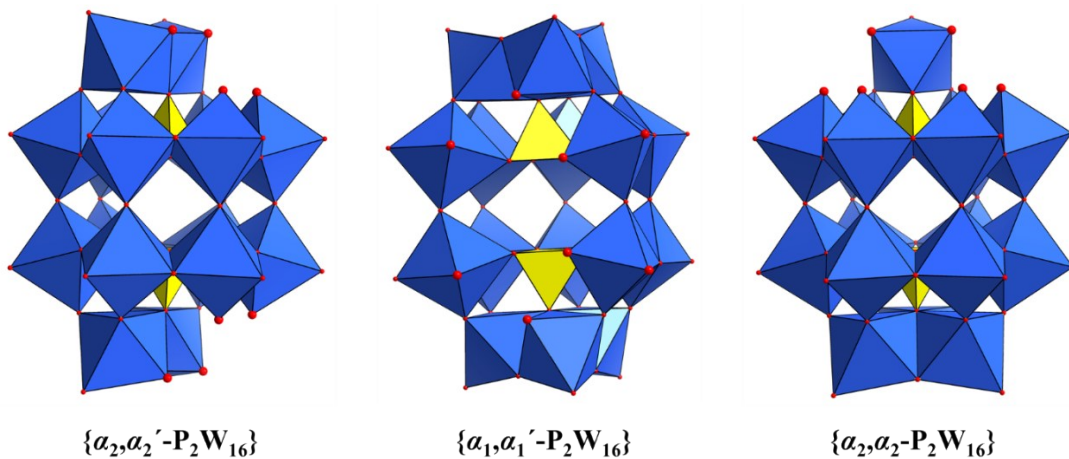


**Figure S7.** Different isomers of the lacunary  $\{P_2W_{16}\}$  derivatives of Wells-Dawson-type POT. Left: the bis-lacunary  $[\alpha_2, \alpha_2'-P_2W_{16}O_{60}]^{14-}$  ( $\{\alpha_2, \alpha_2'-P_2W_{16}\}$ ) with two separate lacuna sites, described in this work. Center and right: the dilacunary  $[\alpha_1, \alpha_1'-P_2W_{16}O_{59}]^{12-}$  ( $\{\alpha_1, \alpha_1'-P_2W_{16}\}$ ) and  $[\alpha_2, \alpha_2-P_2W_{16}O_{59}]^{12-}$  ( $\{\alpha_2, \alpha_2-P_2W_{16}\}$ ) with two directly joined lacuna sites. Color code:  $\{PO_4\}$ : yellow tetrahedra,  $\{WO_6\}$ : blue octahedra;  $O$ : red spheres.

**Table S3.** Summary of the known POT derivatives based on dilacunary Wells-Dawson-type phosphotungstates  $\{\text{P}_2\text{W}_{16}\}^*$

Polyanion	Precursor	pH (if provided)	Reference
<b><math>\{\alpha_2, \alpha_2\text{-P}_2\text{W}_{16}\}</math> derivatives</b>			
$[\alpha_2, \alpha_2\text{-P}_2\text{W}_{16}\text{V}_2\text{O}_{62}]^{8-}$	$[\alpha_2\text{-P}_2\text{W}_{17}\text{O}_{61}]^{10-}$	–	Contant (1991) [6]
$[\text{Zr}_4(\alpha_2, \alpha_2\text{-P}_2\text{W}_{16}\text{O}_{59})_2(\mu_3\text{-O})_2(\text{OH})_2(\text{H}_2\text{O})_4]^{14-}$	$[\alpha\text{-P}_2\text{W}_{15}\text{O}_{56}]^{12-}$	–	M. T. Pope (2003) [7]
$[\text{Zr}^{\text{IV}}_3(\alpha\text{-P}_2\text{W}_{15}\text{O}_{55})(\mu_3\text{-O})(\text{H}_2\text{O})(\text{L/D-tartH})[\alpha_2, \alpha_2\text{-P}_2\text{W}_{16}\text{O}_{59}]]^{15-}$	$[\alpha\text{-P}_2\text{W}_{15}\text{O}_{56}]^{12-}$	–	C. L. Hill (2005) [8]
$[\text{Zr}_2\{(\alpha_2, \alpha_2\text{-P}_2\text{W}_{16}\text{O}_{59})(\mu_3\text{-O})(\text{mal})\}_2]^{18-}$ (mal = L- or D-malate)	$[\alpha\text{-P}_2\text{W}_{15}\text{O}_{56}]^{12-}$	–	C. L. Hill (2005) [9]
$[\text{Zr}^{\text{IV}}_4(\mu_3\text{-O})_2(\mu\text{-O}_2)_2(\text{OAc})_2(\alpha_2, \alpha_2\text{-P}_2\text{W}_{16}\text{O}_{59})_2]^{18-}$	$[\alpha\text{-P}_2\text{W}_{15}\text{O}_{56}]^{12-}$	4.8	Y. Wang, Y. Li (2013) [10]
$[\text{Zr}^{\text{IV}}_4(\mu_3\text{-O})_2(\text{Mal})_2(\text{H}_2\text{O})_2(\alpha_2, \alpha_2\text{-P}_2\text{W}_{16}\text{O}_{59})_2]^{16-}$	$[\alpha\text{-P}_2\text{W}_{15}\text{O}_{56}]^{12-}$	4.5	
$[\text{Hf}_4(\mu_3\text{-O})_2(\mu\text{-OH})_2(\text{H}_2\text{O})_4(\alpha_2, \alpha_2\text{-P}_2\text{W}_{16}\text{O}_{59})_2]^{14-}$	$[\alpha\text{-P}_2\text{W}_{15}\text{O}_{56}]^{12-}$	1.2	K. Nomiya (2009) [11]
$[\{\text{Ce}^{\text{IV}}\text{Mn}^{\text{IV}}\text{O}_9(\text{O}_2\text{CCH}_3)_8\}\{\alpha_2, \alpha_2\text{-P}_2\text{W}_{16}\text{O}_{57}(\text{OH})_2\}]^{8-}$	$[\alpha\text{-P}_2\text{W}_{15}\text{O}_{56}]^{12-}$	acidic	P. Kögerler (2008) [12]
$[\text{Ce}^{\text{IV}}_7\text{Ce}^{\text{III}}_3\text{O}_6(\alpha_2, \alpha_2\text{-P}_2\text{W}_{16}\text{O}_{59})_3(\text{OH})_6(\text{CO}_3)(\text{H}_2\text{O})_{11}]^{19-}$	$[\alpha\text{-P}_2\text{W}_{15}\text{O}_{56}]^{12-}$	7.8	J. Niu, J. Wang (2016) [13]
$[\text{Ce}^{\text{III}}_3(\text{H}_2\text{O})_6(\alpha_2, \alpha_2\text{-P}_2\text{W}_{16}\text{O}_{59})_2]^{15-}$	$[\alpha\text{-P}_2\text{W}_{15}\text{O}_{56}]^{12-}$	7.4	P. Ma, J. Niu (2018) [14]
$[\text{Co}^{\text{II}}_2(\alpha_2, \alpha_2\text{-P}_2\text{W}_{16}\text{O}_{57})_2]^{6-}$	$[\alpha\text{-P}_2\text{W}_{15}\text{O}_{56}]^{12-}$	2.05	Sun (2016) [15]
$[\text{Co}_3\text{H}_2(\alpha_2, \alpha_2\text{-P}_2\text{W}_{16}\text{O}_{57})(\alpha\text{-P}_2\text{W}_{15}\text{O}_{56})(\text{H}_2\text{O})]^{6-}$	$[\alpha\text{-P}_2\text{W}_{15}\text{O}_{56}]^{12-}$	1.84	
<b><math>\{\alpha_1, \alpha_1'\text{-P}_2\text{W}_{16}\}</math> derivatives</b>			
$[\text{Ce}_4^{\text{III}}(\text{OH})_9(\text{OH})_2(\alpha_1, \alpha_1'\text{-P}_2\text{W}_{16}\text{O}_{59})_2]^{14-}$	$[\alpha\text{-H}_2\text{P}_2\text{W}_{12}\text{O}_{48}]^{12-}$	7.3	M. T. Pope (2000) [16]
$[\text{Ce}_3\text{Mn}_2\text{O}_6(\text{OAc})_6(\text{H}_2\text{O})_9]_2[\alpha_1, \alpha_1'\text{-Mn}_2(\text{P}_2\text{W}_{16}\text{O}_{60})]^{20-}$	$[\alpha\text{-H}_2\text{P}_2\text{W}_{12}\text{O}_{48}]^{12-}$	4.0	Y.-H. Wang, E.-B. Wang (2009) [17]
$[\text{Kc}(\alpha_1, \alpha_1' \text{ (or } \alpha_1, \alpha_1) \text{-P}_2\text{W}_{16}\text{Co}^{\text{III}}_2\text{O}_{60})_3]^{23-}$	$[\alpha\text{-P}_2\text{W}_{18}\text{O}_{62}]^{6-}$ **	7.0	Cronin (2009) [18]
$\text{Ti}_6(\text{C}_2\text{O}_4)_4(\alpha_1, \alpha_1'\text{-P}_2\text{W}_{16}\text{O}_{62})_2]^{20-}$	$[\alpha\text{-H}_2\text{P}_2\text{W}_{12}\text{O}_{48}]^{12-}$	1.0	Kortz (2014) [19]
<b><math>\{\alpha_2, \alpha_2'\text{-P}_2\text{W}_{16}\}</math> derivatives</b>			
$[\{(\text{H}_2\text{O})_8\text{Dy}^{\text{III}}_2(\alpha_2, \alpha_2'\text{-P}_2\text{W}_{16}\text{O}_{60})(\text{C}_6\text{H}_5\text{PO})_2\}_2]^{8-}$	$[\alpha_2\text{-P}_2\text{W}_{17}\text{O}_{61}(\text{C}_6\text{H}_5\text{PO})_2]^{10-}$	2.3	This work
$[\{(\text{H}_2\text{O})_{8.25}\text{Y}^{\text{III}}_2(\alpha_2, \alpha_2'\text{-P}_2\text{W}_{16}\text{O}_{60})(\text{C}_6\text{H}_5\text{PO})_2\}_2]^{8-}$		2.3	

\* Only publications reporting on synthesis and primary characterization are mentioned.

\*\* Although the synthesis started from  $[\alpha\text{-P}_2\text{W}_{18}\text{O}_{62}]^{6-}$ , the hexalacunary derivative  $[\alpha\text{-H}_2\text{P}_2\text{W}_{12}\text{O}_{48}]^{12-}$  was synthesized *in situ* in this procedure.

## IV. FT-IR spectroscopy

The FT-IR spectra of **CsK-1** and **CsK-2**, shown on **Figure S8** in comparison with the FT-IR spectra of the phenylphosphonate-functionalized  $K_5H[\alpha_2-P_2W_{17}O_{61}(P(=O)C_6H_5)_2] \cdot 4C_4H_9NO$  ( $K-\{\alpha_2-P_2W_{17}(PhP)_2\}$ ) precursor and the hydrated potassium salt of non-functionalized monolacunary derivatives of Wells-Dawson-type polyanions,  $K_{10}[\alpha_2-P_2W_{17}O_{61}] \cdot 20 H_2O$  ( $K-\{\alpha_2-P_2W_{17}\}$ ), appear to be nearly identical and exhibit characteristic features of the POT moieties and phenylphosphonate groups.

The three bands at 1097, 1061 and 1025  $cm^{-1}$  in the spectra of **CsK-1** and **CsK-2** are attributed to vibrations of P–O bonds in the POT units. They are slightly shifted with respect to the corresponding bands at 1092, 1052 and 1020  $cm^{-1}$  in the spectrum of  $K-\{\alpha_2-P_2W_{17}(PhP)_2\}$  and at 1084, 1049 and 1014  $cm^{-1}$  in the spectrum of  $K-\{\alpha_2-P_2W_{17}\}$ , reflecting formation of the additional lacunary site in the bi-functionalized polyanions **1** and **2**. Two additional peaks at 1173 and 1139  $cm^{-1}$  in the spectra of **CsK-1** and **CsK-2** should be assigned to the stretching vibrations of P–O and P–C bonds in the phenylphosphonate groups as they also seen in the spectrum of  $K-\{\alpha_2-P_2W_{17}(PhP)_2\}$  (at 1166 and 1139  $cm^{-1}$ ) and are not present in the spectrum of  $K-\{\alpha_2-P_2W_{17}(PhP)_2\}$ .

The two peaks at about 985 and 940  $cm^{-1}$  belong to vibrations of the terminal W=O bonds and could be compared to the vibrational bands at 976 and 943  $cm^{-1}$  and at 981 and 939  $cm^{-1}$  in the spectra of  $K-\{\alpha_2-P_2W_{17}(PhP)_2\}$  and  $K-\{\alpha_2-P_2W_{17}(PhP)_2\}$ , respectively. The significant shift of these bands further highlights transformation of the POT skeleton upon formation of **1** and **2** from  $\{\alpha_2-P_2W_{17}(PhP)_2\}$  species. The other peaks in the region from 848 to 450  $cm^{-1}$  belong to W–O–W, W–O–P and W–O–M vibrations. The broad band at about 3417–3430  $cm^{-1}$  and the strong peak at around 1619  $cm^{-1}$  in all the spectra reflect stretching and bending vibrations, respectively, of the lattice and coordinated water molecules. A series of small peaks in the range from 1500 to 1300  $cm^{-1}$  feature stretching and bending vibrations of C=C and C–H bonds in the phenyl groups of the phenylphosphonate moieties.

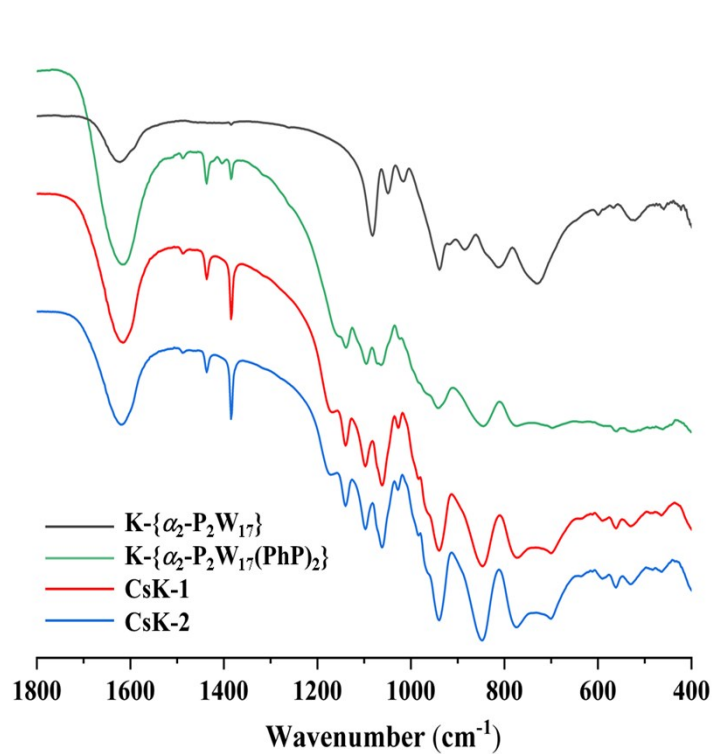


**Figure S8.** FT-IR spectra of CsK-1 (red line) and CsK-2 (blue line) in comparison to those of  $\text{K}_5\text{H}[\alpha_2\text{-P}_2\text{W}_{17}\text{O}_{61}(\text{P}(=\text{O})\text{C}_6\text{H}_5)_2]\cdot 4\text{C}_4\text{H}_9\text{NO}$  ( $\text{K}-\{\alpha_2\text{-P}_2\text{W}_{17}(\text{PhP})_2\}$ ; green line) and  $\text{K}_{10}[\alpha_2\text{-P}_2\text{W}_{17}\text{O}_{61}]\cdot 20\text{H}_2\text{O}$  ( $\text{K}-\{\alpha_2\text{-P}_2\text{W}_{17}\}$ ; black line).

## V. Thermogravimetric analysis

The thermal decomposition processes for **CsK-1** and **CsK-2** were investigated under N<sub>2</sub> atmosphere in the temperature range from room temperature up to 900 °C. The obtained curves, shown on **Figures S9** and **S10**, exhibit a series of smooth overlapping steps which are not easy to precisely separate.

The first group of the overlapping weight loss steps, which starts already at room temperature and could be terminated at about 275 °C based on the weight derivatives curves, corresponds to the removal of both lattice and (at higher temperatures) coordinated water molecules: (9.1 % calculated *vs.* 9.0 % observed for **CsK-1** and 9.3 % calc. *vs.* 8.9 % obs. for **CsK-2**). The slightly smaller than expected (*vs.* the value derived from elemental analysis) water content observed in the TGA of **CsK-2** can be explained by higher degree of dryness of the sample, since some of the crystal water evaporated in dry air at RT due to different drying times.

The subsequent weight loss step(s), occurring from 400 to 650 °C, could be attributed to the decomposition of the phenyl groups in **1** and **2** (2.8 % calc. *vs.* 2.7 % obs. for **CsK-1** and 2.8 % calc. *vs.* 2.8 % obs. for **CsK-2**), which is directly followed by thermal decomposition and rearrangement of the POT skeleton with formation of complex oxide species. The total weight loss at 900 °C constitutes 17.1 % for **CsK-1** and 17.5 % for **CsK-2**.

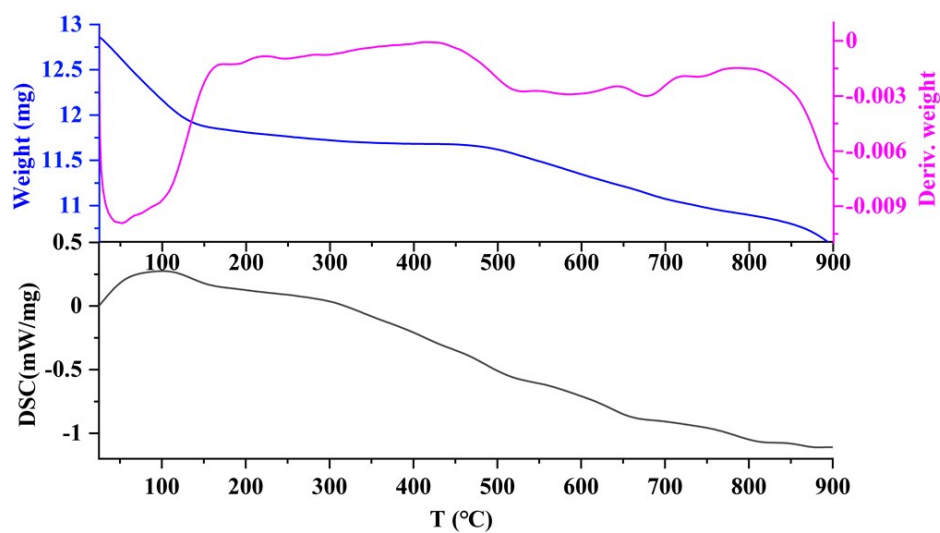


**Figure S9.** TGA (blue), weight derivative (green) and DSC (black) curves for **CsK-1** from room temperature to 900 °C under N<sub>2</sub> atmosphere.

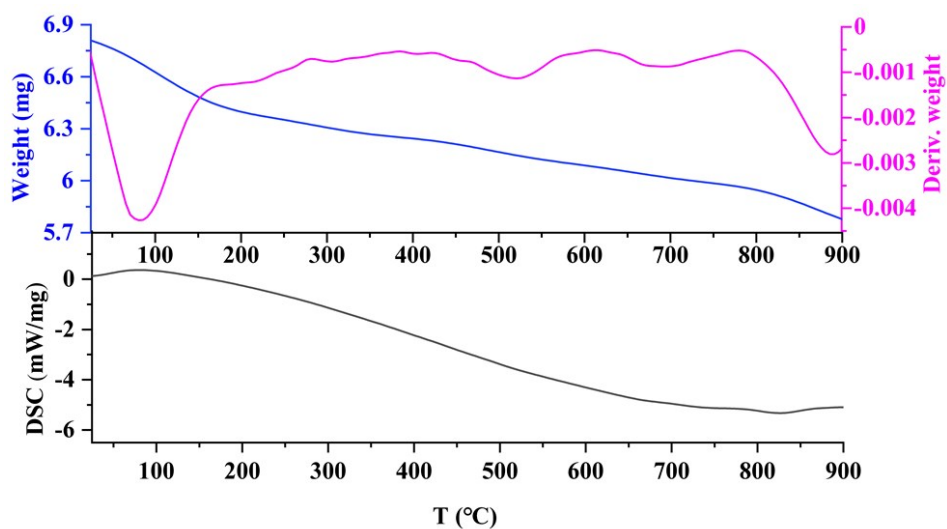


**Figure S10.** TGA (blue), weight derivative (green) and DSC (black) curves for **CsK-2** from room temperature to 900 °C under N<sub>2</sub> atmosphere.

## VI. NMR spectroscopy

$^1\text{H}$  and  $^{31}\text{P}$  NMR spectra of the diamagnetic derivative **CsK-2** were measured in  $\text{D}_2\text{O}$  at room temperature. Due to the poor solubility of the compound,  $\text{Li}^+$ -loaded ion exchange resin (Dowex 50) was used to increase concentration of **2** in the solution. \*

$^{31}\text{P}$  NMR spectrum of **2** (**Figure S11**) exhibits three signals in a full agreement with the structural data for **CsK-2**. Two of them, at  $-8.04$  and  $-12.05$  ppm with relative intensities of 1 : 1, belong to the symmetrically independent P centers of the  $\{\alpha_2, \alpha_2' - \text{P}_2\text{W}_{16}\text{O}_{60}\}^{14-}$  moieties in **2**. The downfield signal at 16.21 ppm could be attributed to the P centers of the phenylphosphonate groups. The spectrum remains unchanged for at least several hours, while after that additional signals start to appear indicating a start of a slow decomposition of the polyanions **2**. In particular, a sharp singlet at 14.22 ppm is clearly seen in the spectrum measured after 72 h after dissolution of **CsK-2** and its intensity increases in the spectrum recorded after 1 week. The growth of this singlet is accompanied with an appearance of a series of small signals in the negative ppm area attributed to P atoms in POTs. This suggests that the decomposition of polyanions **2** proceeds via dissociation of  $\{(\text{C}_6\text{H}_5\text{PO})_2\text{Y}(\text{H}_2\text{O})_x\}^{6+}$  moieties leading to destabilization and rearrangement of the POT skeleton. Therefore, the singlet at 14.22 ppm can either be attributed to free phenylphosphonate ions or to a symmetrical  $\text{Y}^{\text{III}}$  phenylphosphonate complex which is hard to unambiguously judge as the exact position of the  $^{31}\text{P}$  NMR signal for P atom in phenylphosphonates is very sensitive to pH and cationic composition of the solution. Nevertheless, the amount of intact polyanions **2** in aqueous medium remain quite high even after one week (see **Figure S11**).

The  $^1\text{H}$  NMR spectrum of polyanion **2** (**Figure S12**) does not show a clear pattern, which would be expected for the phenyl groups, even directly after the dissolution of **CsK-2** in  $\text{D}_2\text{O}$ . The reason for it is most likely the fact the coordination of  $\text{Y}^{\text{III}}$  ion to the O atoms of the phenylphosphonate groups could make protons of the phenyl rings located in the ortho and para with respect to the P atom positions symmetrically inequivalent (one located more closely to the  $\text{Y}^{\text{III}}$  ion and another one pointed towards the POT moiety). Another explanation could be partial dissociation of the

---

\* It was also controlled that the  $\text{Li}^+$ -loaded resin gave pH 2.3 when placed in water before addition of **CsK-2** to prevent polyanions decomposition.

only weakly bound to the terminal oxygens of the phenylphosphonates  $Y^{III}$  ions. In agreement to the  $^{31}\text{P}$  NMR measurement, additional signals start to appear after 1 day reflecting release of organophosphonate groups from the polyanions.

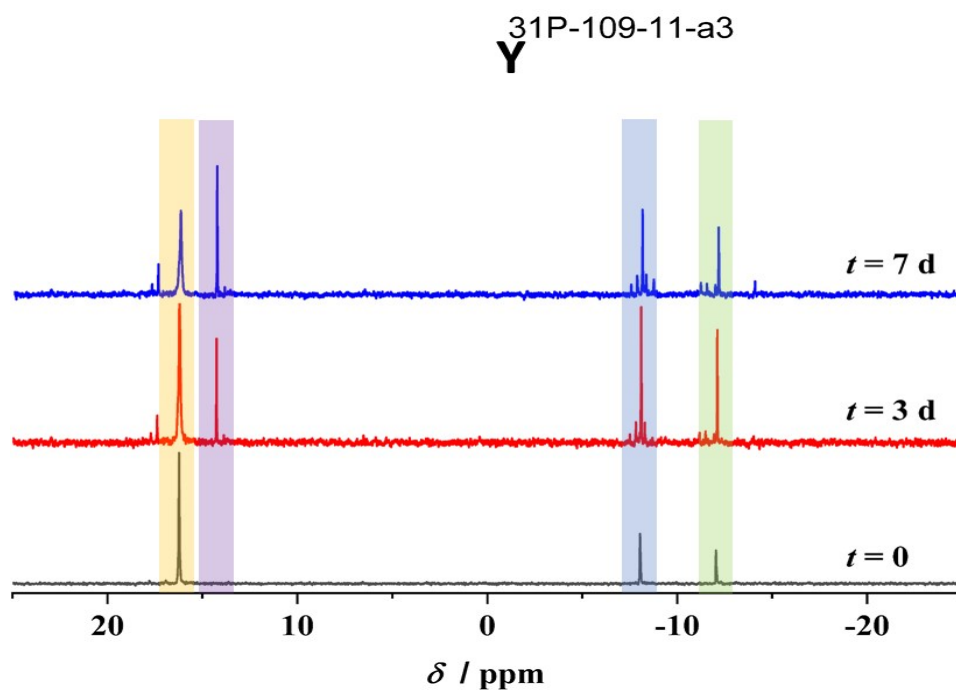


**Figure S11.** Room-temperature time-dependent  $^{31}\text{P}$  NMR spectra of **2** in  $\text{D}_2\text{O}$ .

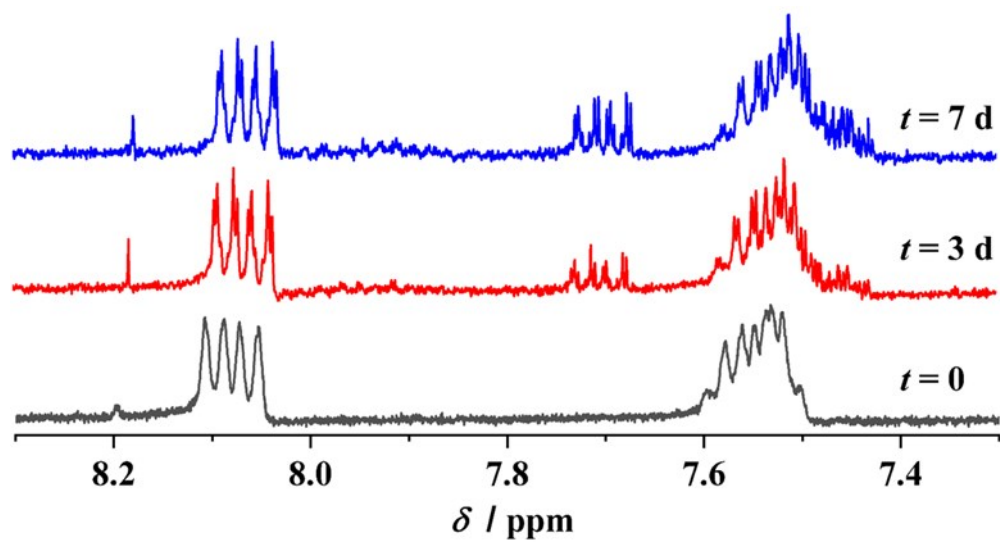


**Figure S12.** Room-temperature time-dependent <sup>1</sup>H NMR spectra of polyanions **2** in D<sub>2</sub>O.

## VII. UV-Vis spectroscopy

The UV-Vis spectra of **CsK-1** (**Figure S13**, left) and **CsK-2** (**Figure S14**, left) in 0.5 M Li<sub>2</sub>SO<sub>4</sub> (pH 2.5) show similar characteristics. They exhibit a strong absorption maximum at 200 nm ( $\epsilon = 3.68 \times 10^5 \text{ M}^{-1}\text{cm}^{-1}$  for **1** and  $3.68 \times 10^5 \text{ M}^{-1}\text{cm}^{-1}$  for **2**), which is followed by a shoulder at around 260 nm ( $\epsilon = 7.82 \times 10^4 \text{ M}^{-1}\text{cm}^{-1}$  for **1** and  $9.14 \times 10^4 \text{ M}^{-1}\text{cm}^{-1}$  for **2**), both associated with oxygen-to-metal charge transfer processes.

The time-dependent measurements were performed on diluted solutions of **CsK-1** (**Figure S13**, right) and **CsK-2** (**Figure S14**, right) in the same medium (see the exact concentrations in the figure captures). These stability tests showed that the spectra of the solutions remain unchanged for at least one day suggesting the stability of the polyanions **1** and **2** in this medium. These data are also in line with the NMR data on aqueous solutions.

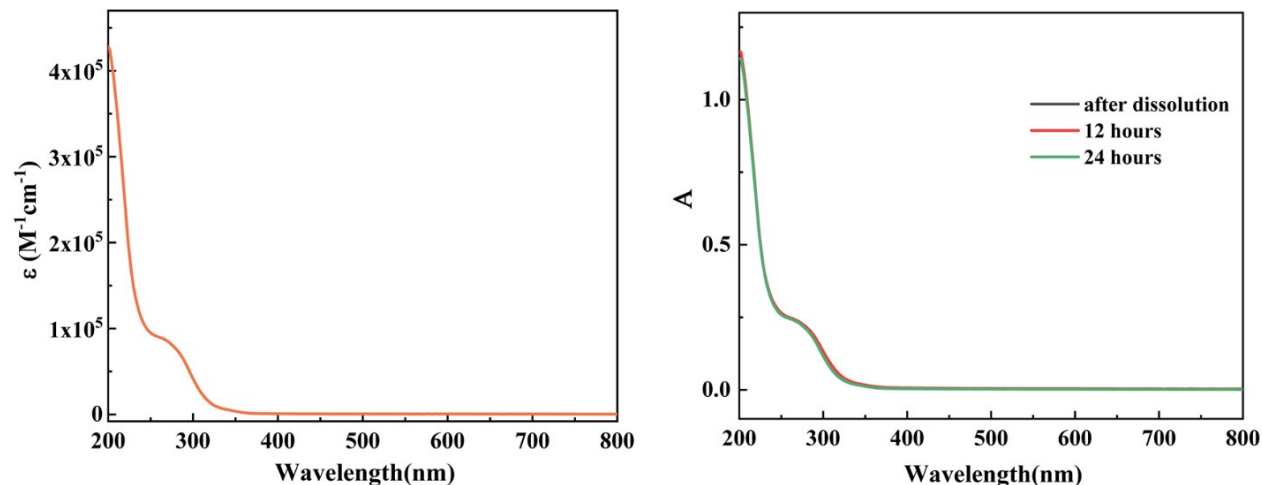


**Figure S13.** Left: room-temperature UV-Vis spectrum of **1** in 0.5 M  $\text{Li}_2\text{SO}_4$  (pH 2.5) ( $\epsilon$  values are averaged from the spectra of the solutions with concentrations between  $1.5 \times 10^{-6}$  and  $3.0 \times 10^{-6}$  M). Right: time-dependent UV-Vis spectrum of **1** in 0.5 M  $\text{Li}_2\text{SO}_4$  (pH 2.5),  $c = 2.7 \times 10^{-6}$  M.

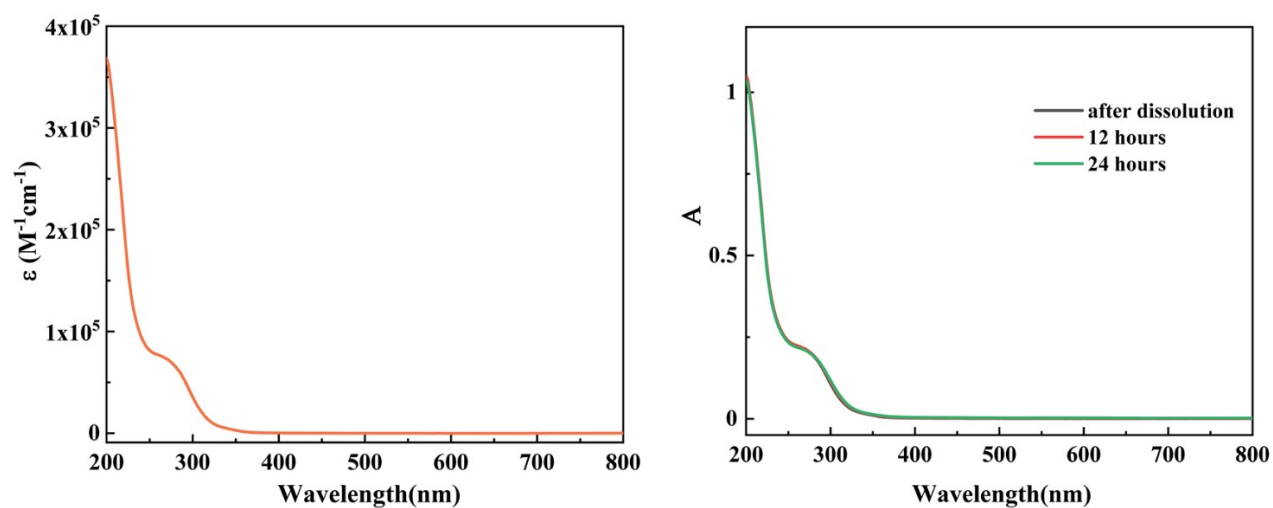


**Figure S14.** Left: room-temperature UV-Vis spectrum of **2** in 0.5 M  $\text{Li}_2\text{SO}_4$  (pH 2.5) ( $\epsilon$  values are averaged from the spectra of the solutions with concentrations between  $2.2 \times 10^{-6}$  and  $2.8 \times 10^{-6}$  M). Right: time-dependent UV-Vis spectrum of **2** in 0.5 M  $\text{Li}_2\text{SO}_4$  (pH 2.5),  $c = 2.8 \times 10^{-6}$  M.

## VIII. Electrochemical studies

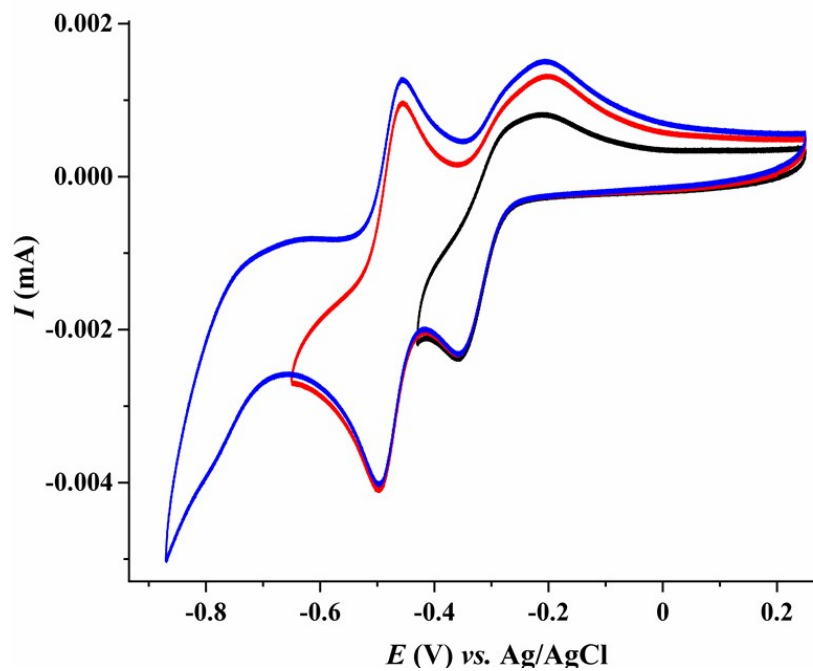


**Figure S15.** Room-temperature cyclic voltammograms of saturated **CsK-1** solution in 1.0 M LiOAc buffer (pH 3.8) with different negative potential limits (-0.43 V, -0.65 V, -0.87 V) at scan rate of 20 mV/s.

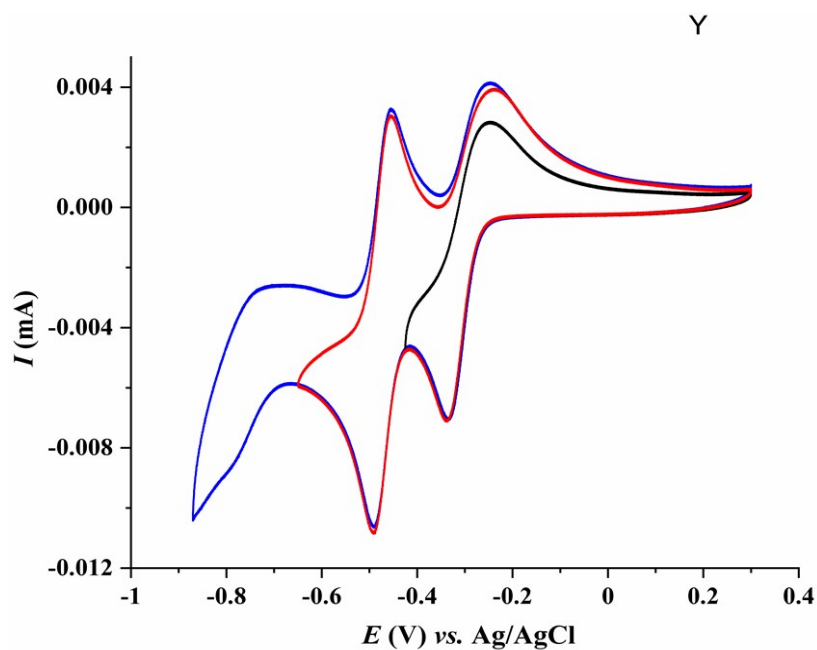


**Figure S16.** Room-temperature cyclic voltammograms of saturated **CsK-2** solution in 1.0 M LiOAc buffer (pH 3.8) with different negative potential limits ( $-0.425$  V,  $-0.65$  V,  $-0.87$  V) at scan rate of 20 mV/s.

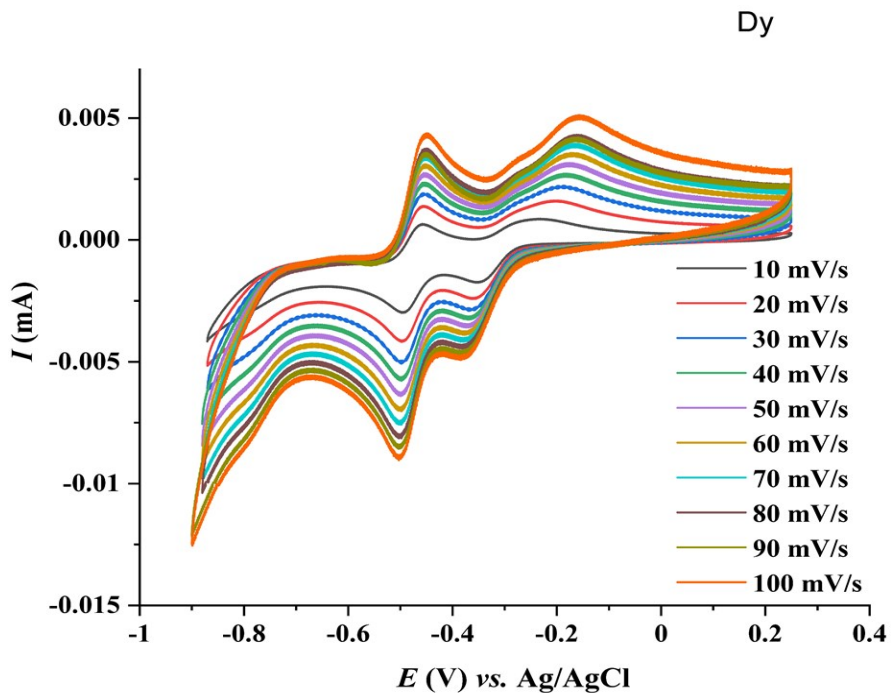


**Figure S17.** Room-temperature cyclic voltammograms of a saturated **CsK-1** solution in 1.0 M LiOAc buffer (pH 3.8) at different scan rates.

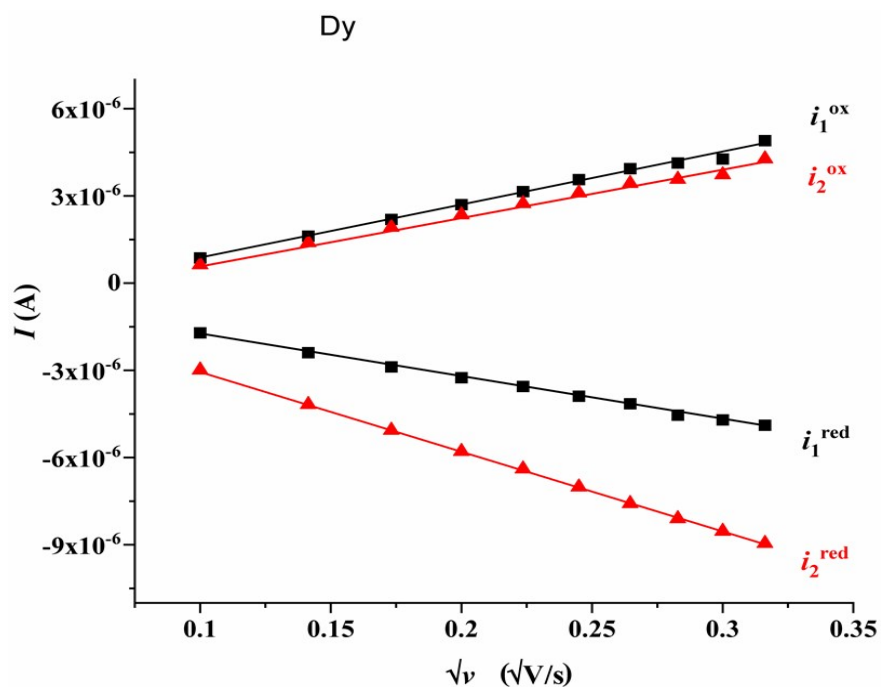


**Figure S18.** Dependence of peak currents from square root of the scan rate for **CsK-1**, see **Table S4**.

**Table S4.** Values of redox peaks potentials and currents depending on the scan rate for **CsK-1**.

Scan rate / $\text{mV s}^{-1}$	1 <sup>st</sup> redox couple					
	$E_p^c / \text{V}$	$i_p^c / \mu\text{A}$	$E_p^a / \text{V}$	$i_p^a / \mu\text{A}$	$E_{1/2} / \text{V}$	$\Delta E / \text{V}$
10	-0.23	0.867	-0.345	-1.71	-0.29	-0.059
20	-0.20	1.62	-0.355	-2.39	-0.28	-0.075
30	-0.19	2.19	-0.36	-2.88	-0.275	-0.084
40	-0.18	2.70	-0.36	-3.26	-0.27	-0.091
50	-0.175	3.15	-0.37	-3.55	-0.27	-0.096
60	-0.17	3.56	-0.37	-3.89	-0.27	-0.10
70	-0.165	3.94	-0.375	-4.15	-0.27	-0.11
80	-0.16	4.13	-0.38	-4.54	-0.27	-0.11
90	-0.16	4.27	-0.385	-4.70	-0.27	-0.11
100	-0.15	5.11	-0.39	-4.89	-0.27	-0.12

Scan rate / $\text{mV s}^{-1}$	2 <sup>nd</sup> redox couple					
	$E_p^c / \text{V}$	$i_p^c / \mu\text{A}$	$E_p^a / \text{V}$	$i_p^a / \mu\text{A}$	$E_{1/2} / \text{V}$	$\Delta E / \text{V}$
10	-0.46	0.63	-0.49	-2.99	-0.48	-0.017
20	-0.46	1.39	-0.495	-4.18	-0.48	-0.019
30	-0.46	1.92	-0.50	-5.06	-0.48	-0.020
40	-0.46	2.35	-0.50	-5.79	-0.48	-0.021
50	-0.455	2.74	-0.50	-6.39	-0.48	-0.022
60	-0.45	3.11	-0.50	-7.01	-0.48	-0.023
70	-0.45	3.43	-0.50	-7.58	-0.48	-0.024
80	-0.45	3.57	-0.50	-8.10	-0.48	-0.025
90	-0.45	3.73	-0.50	-8.54	-0.48	-0.026
100	-0.45	4.38	-0.50	-8.95	-0.48	-0.0265

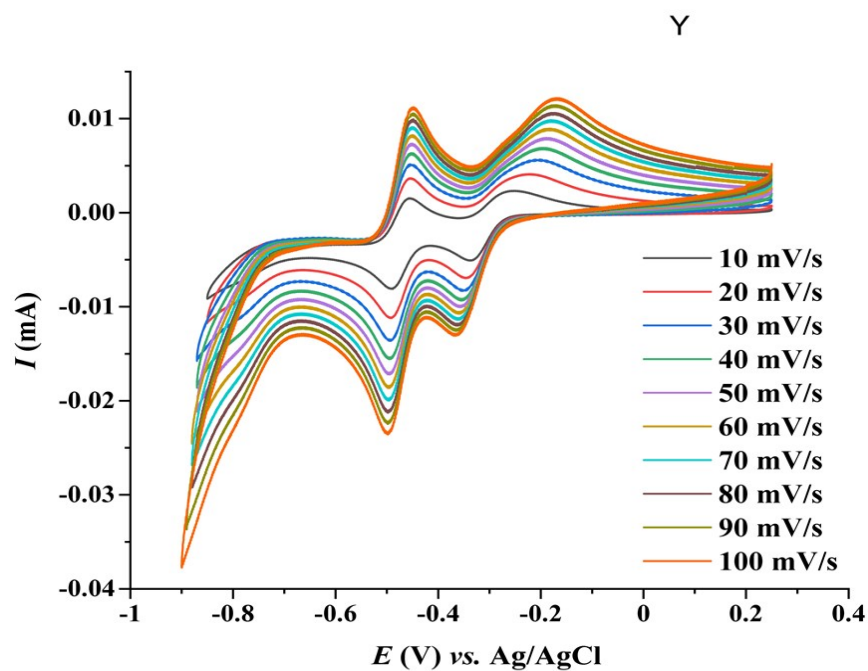


**Figure S19.** Room-temperature cyclic voltammograms of a saturated CsK-2 solution in 1.0 M LiOAc buffer solution (pH 3.8) at different scan rates.

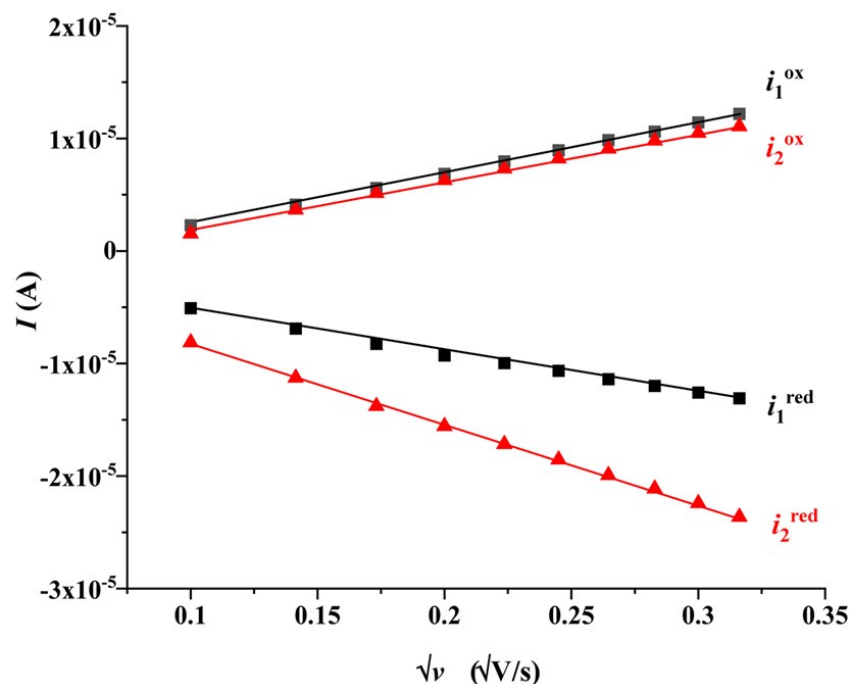


**Figure S20.** Dependence of peak currents from square root of the scan rate of **CsK-2**, see **Table S5**.

**Table S5.** Values of redox peaks potentials and currents depending on the scan rate for **CsK-2**.

Scan rate / $\text{mV s}^{-1}$	1 <sup>st</sup> redox couple					
	$E_p^c / \text{V}$	$i_p^c / \mu\text{A}$	$E_p^a / \text{V}$	$i_p^a / \mu\text{A}$	$E_{1/2} / \text{V}$	$\Delta E / \text{V}$
10	-0.34	-5.08	-0.25	2.33	-0.29	0.042
20	-0.34	-6.89	-0.22	4.11	-0.28	0.062
30	-0.35	-8.26	-0.20	5.62	-0.28	0.072
40	-0.35	-9.28	-0.19	6.89	-0.27	0.081
50	-0.36	-9.97	-0.19	7.94	-0.27	0.084
60	-0.36	-10.65	-0.18	8.95	-0.27	0.089
70	-0.36	-11.40	-0.18	9.85	-0.27	0.091
80	-0.36	-11.99	-0.18	10.61	-0.27	0.093
90	-0.36	-12.59	-0.17	11.43	-0.27	0.096
100	-0.37	-13.09	-0.17	12.19	-0.27	0.098

Scan rate / mV s <sup>-1</sup>	2 <sup>nd</sup> redox couple					
	$E_p^c$ / V	$i_p^c$ / $\mu$ A	$E_p^a$ / V	$i_p^a$ / $\mu$ A	$E_{1/2}$ / V	$\Delta E$ / V
10	-0.49	-8.09	-0.455	1.53	-0.47	0.017
20	-0.49	-11.21	-0.45	3.68	-0.47	0.0185
30	-0.49	-13.63	-0.45	5.14	-0.47	0.019
40	-0.49	-15.57	-0.45	6.28	-0.47	0.020
50	-0.49	-17.21	-0.45	7.33	-0.47	0.021
60	-0.50	-18.65	-0.45	8.22	-0.47	0.0215
70	-0.50	-19.81	-0.45	9.91	-0.47	0.022
80	-0.50	-21.04	-0.45	9.80	-0.47	0.023
90	-0.50	-22.47	-0.45	10.49	-0.475	0.024
100	-0.50	-23.58	-0.45	11.07	-0.475	0.024

## IX. Magnetochemical studies

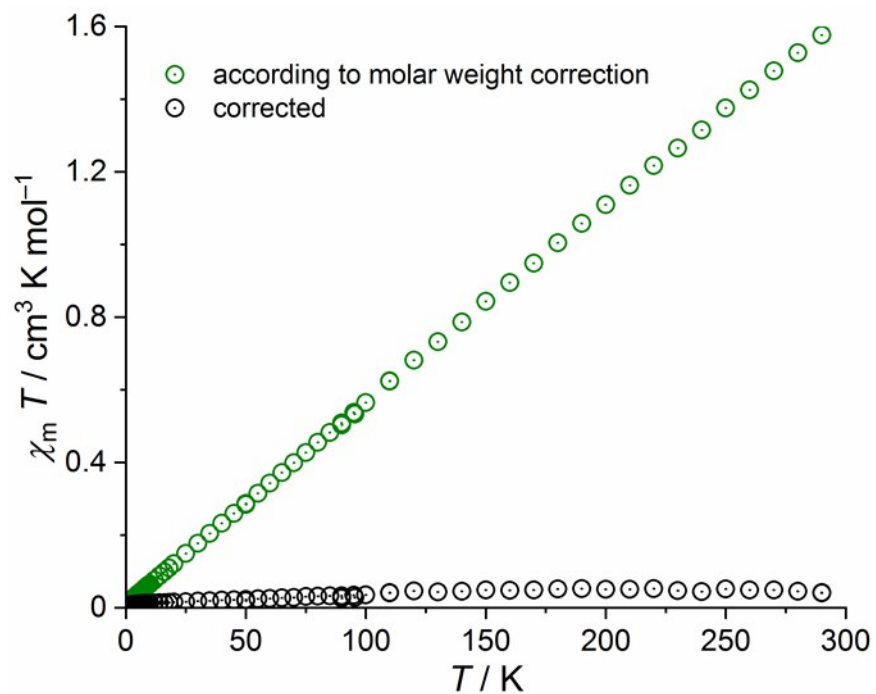


**Figure S21.** Estimation of the correct intrinsic diamagnetic contribution of the polyoxotungstate. POTs, or polyoxometalates in general, are well known to exhibit a TIP-like behavior in case of the diamagnetic contribution is determined by Pascal's constants or the molar weight method, even if they are fully oxidized. This may be due to presence of a TIP (temperature independent paramagnetism) or an over-estimation of the diamagnetic contribution that may be intrinsic to these methods. Thus, the correction of  $\chi_{m, \text{diacorr}} = +5.23 \times 10^{-3} \text{ cm}^3 \text{ mol}^{-1}$  (converting green to black symbols) was applied to all data.

The *ac* susceptibility of compound **CsK-1** was also tested for slow relaxation processes, which are an indicator of potential SMMs. We applied small static bias fields to improve the curvatures of Cole-Cole plots, since only weak out-of-phase signals are observed at zero static bias field. The best result is achieved at a static field of 600 Oe. Fitting the data to a generalized Debye expression,<sup>[20]</sup> i. e. simultaneously fitting  $\chi_m''$  vs. frequency  $f$  and  $\chi_m'$  vs.  $f$ , yields the average relaxation times of magnetization  $\tau$  shown in Fig. S22 (right) with the spread  $\alpha$  in the range 0.27–0.53. However, the Arrhenius plot of  $\tau$  vs.  $1/T$  reveals a zigzag curve instead of continuously increasing values of  $\tau$  with increasing  $1/T$ . Instead of observing a single set of slow relaxation processes (Orbach, Raman, etc.), from which each process is dominant at certain temperatures, such a rather infrequent behavior appears if a set of relaxation processes changes from one to another set depending on the applied temperature.

Due to this and in order to avoid over-parametrization, solely both increasing parts of the curve are fitted to the Arrhenius expression  $\tau = \tau_0 \times \exp(-U_{\text{eff}}/(k_B T))$  describing an Orbach-type relaxation process, where  $\tau_0$  is the attempt time,  $U_{\text{eff}}$  the effective barrier and  $k_B$  Boltzmann's constant. For the low-temperature range (red line in Fig. S22, right), the least-squares fit yields  $\tau_0 = (1.9 \pm 3.2) \times 10^{-9}$  s and  $U_{\text{eff}} = (12.2 \pm 2.2)$  cm<sup>-1</sup>, while for the higher temperature range (blue line)  $\tau_0 = (9.7 \pm 2.2) \times 10^{-6}$  s and  $U_{\text{eff}} = (8.0 \pm 0.8)$  cm<sup>-1</sup> are determined. The obtained effective barriers for **CsK-1** and attempt times are rather small, yet common for similar compounds.<sup>[21]</sup>

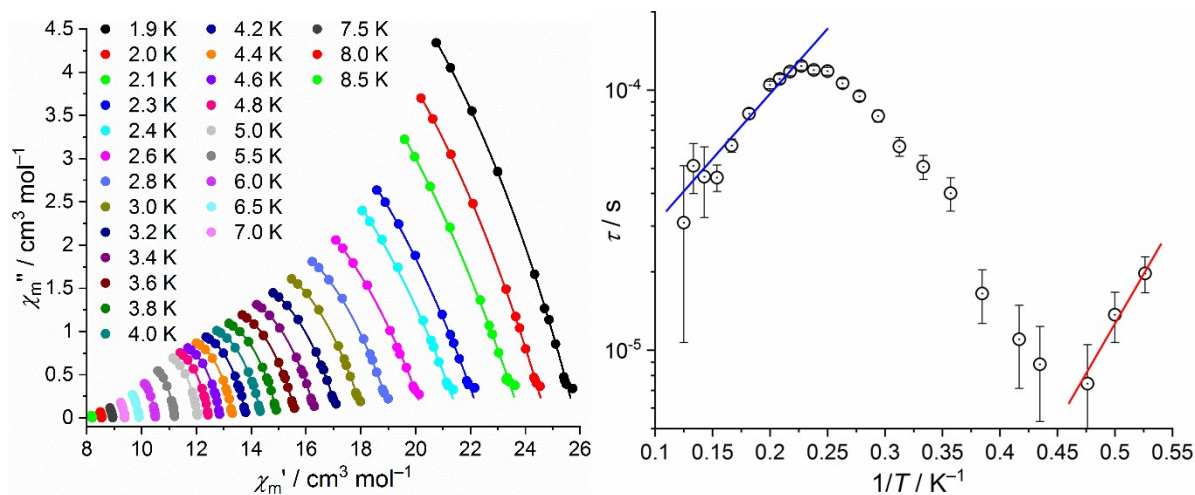


**Figure S22.** Dynamic magnetic properties of CsK-1 at a static bias field of 600 Oe: (a) out-of-phase  $\chi_m''$  vs. in-phase magnetic susceptibility  $\chi_m'$  (data: symbols, fit to Debye expression: solid lines); (b) Arrhenius plot of average relaxation times of magnetization  $\tau$  vs. inverse temperature  $1/T$  (data (with statistical error bars): symbols, solid lines: fit to Arrhenius expressions).

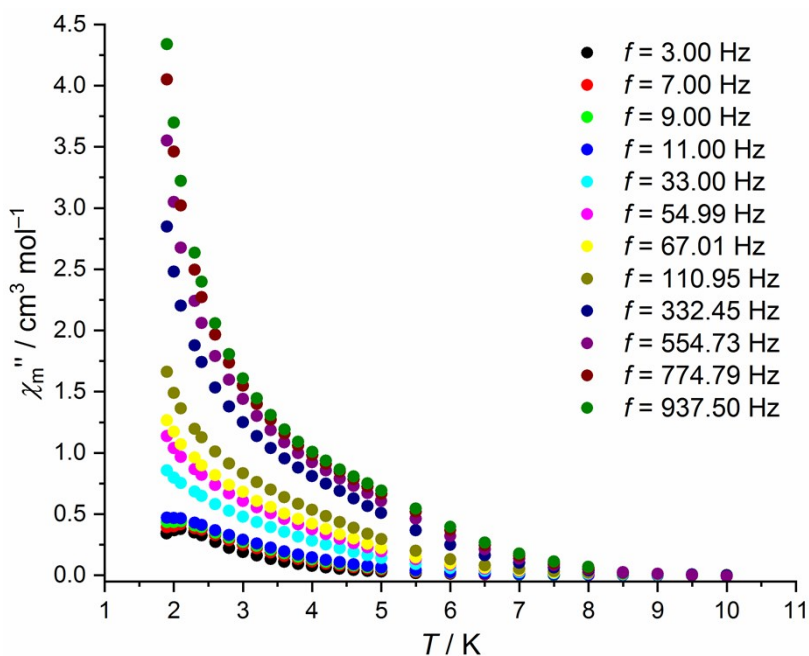


**Figure S23.** Temperature dependence of the out-of-phase susceptibility component  $\chi_m''$  for ac frequencies from 3 to 937.5 Hz, recorded at a static bias field of 600 Oe.

## X. References

- [1] R. Contant, W. G. Klemperer, O. Yaghi, *Inorg. Synth.* **1990**, *27*, 104–111.
- [2] S. Fujimoto, J. M. Cameron, R.-J. Wei, K. Kastner, D. Robinson, V. Sans, G. N. Newton, H. Oshio, *Inorg. Chem.* **2017**, *56*, 12169–12177.
- [3] STOE X-Red32, absorption correction by Gaussian integration, analogous to P. Coppens, The Evaluation of Absorption and Extinction in Single-Crystal Structure Analysis. Crystallographic Computing (Ed.: F. R. Ahmed), Munksgaard, Copenhagen, **1970**, pp. 255–270.
- [4] J. Koziskova, F. Hahn, J. Richter, J. Kožišek, *Acta Chim. Slov.* **2016**, *9*, 136–140.
- [5] G. M. Sheldrick, *Acta Cryst.* **2015**, *C71*, 3–8.
- [6] M. Abbessi, R. Contant, R. Thouvenot, G. Herve, *Inorg. Chem.* **1991**, *30*, 1695–1702.
- [7] A. J. Gaunt, I. May, D. Collison, K. T. Holman, M. T. Pope, *J. Mol. Struct.* **2003**, *656*, 101–106.
- [8] X. Fang, T. M. Anderson, C. L. Hill, *Angew. Chem. Int. Ed.* **2005**, *44*, 3540–3544.
- [9] X. Fang, T. M. Anderson, Y. Hou, C. L. Hill, *Chem. Commun.* **2005**, 5044–5046.
- [10] D. Li, H. Han, Y. Wang, X. Wang, Y. Li, E. Wang, *Eur. J. Inorg. Chem.* **2013**, 1926–1934.
- [11] Y. Saku, Y. Sakai, K. Nomiya, *Inorg. Chem. Commun.* **2009**, *12*, 650–652.
- [12] X. Fang, P. Kögerler, *Chem. Commun.* **2008**, 3396–3398.
- [13] P. Ma, R. Wan, Y. Wang, F. Hu, D. Zhang, J. Niu, J. Wang, *Inorg. Chem.* **2016**, *55*, 918–924.
- [14] H. Wu, X. Meng, R. Wan, P. Ma, J. Wang, J. Niu, *Inorg. Chem. Comm.* **2018**, *95*, 154–157.
- [15] L.-Y. Guo, M. Jagodič, S.-Y. Zeng, Z. Wang, Z.-Q. Shi, X.-P. Wang, C.-H. Tung, D. Sun, *Dalton Trans.* **2016**, *45*, 8404–8411.
- [16] A. Ostuni, M. T. Pope, *Compt. Rend. Acad. Sci. II C* **2000**, *3*, 199–204.
- [17] Y.-W. Li, Y.-G. Li, Y.-H. Wang, X.-J. Feng, Y. Lu, E.-B. Wang, *Inorg. Chem.* **2009**, *48*, 6452–6458.
- [18] S. G. Mitchell, S. Khanra, H. N. Miras, T. Boyd, D.-L. Long, L. Cronin, *Chem. Commun.* **2009**, 2712–2714.
- [19] G. Al-Kadamany, B. S. Bassil, F. Raad, U. Kortz, *J. Clust. Sci.* **2014**, *25*, 867–878.
- [20] K. S. Cole, R. H. Cole, *J. Chem. Phys.* **1941**, *9*, 341–351
- [21] D. N. Woodruff, R. E. Winpenny, R. A. Layfield, *Chem. Rev.* **2013**, *113*, 5110–5148.